Nonlinear Wavefield Characteristics of Seismic Translation and Rotation in Small-Strain Deformation~~: Insights~~ from Moment Tensor Simulations

Wei Li [1,2], Yun Wang [1,2,*], Chang Chen[1,2], Lixia Sun[1,3]

[1] *"MWMC" group, School of Geophysics and Information Technology, China University of Geosciences, Beijing* 100083*, China*

[2] *State Key Laboratory of Geological Processes and Mineral Resources, China University of Geosciences, Beijing* 100083*, China*

[3] *Sinopec Research Institute of Petroleum Engineering Co., Ltd., Beijing* 102206*, China*

[*] Corresponding author: wangyun@mail.gyig.ac.cn.

Abstract Seismic rotational motions recorded in near-field and strong-~~magnitude~~ motion observations show ~~exhibit~~ discrepancies with theoretical predictions derived from linear elastodynamic theory~~principles~~. To investigate ~~explore~~ potential nonlinear contributions ~~to the phenomenon~~, this study incorporates geometric nonlinear ~~strain~~ effects into wave propagation theory using the ~~through~~ Green-Lagrange strain tensor ~~formulations~~. A staggered-grid finite-difference method is used to simulate~~s~~ six-component ~~wavefields~~ (translational and rotational) wavefields generated by three fundamental seismic sources: isotropic (ISO), double-couple (DC), and compensated linear vector dipole (CLVD). The r~~R~~esults demonstrate that nonlinear effects, as a secondary source, have a universal intensity pattern adhering to the physics of wave

motion~~nonlinear effects strongly depend on source characteristics and energy intensity~~. However, the excitation efficiency and modulation of wavefield attributes (such as P-wave polarization) depend strongly on source type ~~ISO sources exhibit uniform nonlinear anomalies from volumetric-shear coupling, CLVD sources amplify directional strain-axis effects, and DC sources amplify localized nonlinearity along faulting directions~~. Simulations show that rotational components exhibit higher sensitivity to nonlinear effects driven by S-waves. Reference simulations of two moderate-to-strong earthquakes suggest that surface waves are the primary carriers of nonlinear features. ~~Rotational components show higher sensitivity to nonlinearity than translational components, which are also contingent on source-receiver geometry. Simulations of two moderate-strong earthquakes highlight surface waves as preferential carriers of nonlinear signatures, though path effects and site amplification require systematic exploration. These results establish a framework for advancing nonlinearity study in ground motion analysis while emphasizing the need for instrumentally resolved rotational measurements and complex media modeling.~~

1 Introduction

Seismic rotational motions is a significant part of ground shaking, particularly recordable in strong-motion eventscan be recorded in ground shaking, especially when caused by strong earthquakes (Graizer, 1991; 2010; Zhou et al., 2019). Under near-field and shallow-source conditions, tThese rotational motions exhibit pronounced characteristics in shallow focal depths and near-field conditions (Kozak, 2009; Sun et al., 2017). Within the domain of structural engineering, the incorporation of rotational analysis has gained increasing recognition for its and play a critical role in the seismic design and stability assessment of structuresassessing ground motion stability and building design (Li, 1991; Li and Sun, 2001; Yan, 2017; Huras et al., 2021). Progress in research indicatesStudies advancements suggest that incorporating seismic rotational motion data, which contains information on the captures spatial gradients of the wavefield, can improve enhance the accuracy and stability of earthquake seismic source characterization and moment tensor inversion (Bernauer et al., 2014; Donner, 2016; Ichinose et al., 2021;), as supported by simulations conducted by Hua and Zhang, (2022).

In a review of advances in rotational seismology,The work of Lee et al. (20097) comprehensively reviewed the applications of seismic rotation observations in seismic engineering, postulatingsuggested that the measured rotational components in strong ground motion may predominantly originate from the nonlinear elasticity and site effects. This suggestion conclusion is based on drawn from empirical evidence from observations in Japan and Taiwan, where showing that actual rotational measurements

are typically one to two orders of magnitude larger than those expected from classical linear elasticity theory or derived from translational data, indicating the limitations of linear theory~~exceed derived rotational components from translational data by 1-2 orders of magnitude~~. In geophysics, nonlinearity often refers to constitutive nonlinearity related to material behavior, such as the hysteretic and elastoplastic responses of soils and rocks under large strains (Bonilla et al., 2005; Bonilla et al., 2011; Frankel et al., 2002; Régnier et al., 2018).~~addressing the complex geophysical phenomena stemming from Earth's heterogeneities, progress has been made in developing analytical solutions for nonlinear wave equations through iterative techniques in Green's function (McCall, 1994).~~ This type of nonlinearity involves intrinsic energy dissipation and plastic deformation, resulting in nonlinear site amplification in strong-motion records (Régnier et al., 2018)~~Notable methodological developments include the flux-corrected transport method (Yang et al., 2002; Zheng et al., 2006) and perturbation approaches (Bataille and Contreras, 2009; Jia et al., 2020), which have been instrumental in investigating nonlinear effects on elastic wave propagation~~.

On the other hand, nonlinearity can also arise from the geometric description of an object's deformation itself, known as geometric nonlinearity. Even if a material adheres to Hooke's law, the mathematical relationship between strain and displacement can still contain higher-order nonlinear terms. This geometric nonlinearity is significant when describing seismic wave propagation in pre-stressed media (Tromp and Trampert, 2018). ~~—~~However, current research ~~studies —~~has

predominantly ~~primarily~~ focused on material ~~nonlinear~~ constitutive nonlinearity ~~relations between stress and strain under small strain~~ and its linearizedation approximation~~s~~ (Renaud et al., 2012; 2013; TenCate et al., 2016; Feng et al., 2018), with a~~,~~ systematic investigation into the strain nonlinearity introduced by the measure of deformation, and its expression in seismic wave propagation, is still lacking.~~leaving a gap in understanding the strain nonlinearity.~~ This neglected aspect may ~~hold~~ contribute~~the key~~ to understanding the complex~~more accurate representations of~~ rotational motions observed in ~~strong earthquakes and~~the near- field of strong earthquakes~~conditions~~.

Therefore, ~~In the seismically active region of Taiwan, broadband seismic observations and physical source studies have revealed significant rotational components in Taiwan's seismic events, demonstrating distinct strike-slip rotation characteristics between the southern and northern regions of the island (Yu et al., 1999; Wang and Lv, 2006). Oliveira and Bolt (1989) estimated rotational components of strong motions, confirming their non-negligible impact in near-field observations across Taiwan. Through analysis of six-component ground motion data from 52 earthquakes recorded at the HGSD station in eastern Taiwan during 2007–2008, Chen et al. (2014) identified substantial vertical rotational motions in proximal seismic locations and notable differences in energy and spectral characteristics between horizontal and vertical rotational motions. These studies show the importance of seismic rotation analysis in elucidating Taiwan's subsurface structures and geodynamic processes.~~

this study aims to systematically characterize geometric nonlinear effects within the framework of the small-strain assumption by incorporating the Green-Lagrange strain tensor.~~In this research, we develop a theoretical and numerical framework for analyzing nonlinear seismic wave propagation through Green strain tensor formulations.~~ We ~~derive velocity-stress equations incorporating nonlinear strain coupling terms,~~ employ a staggered-grid finite-difference method to simulate ~~six-component wavefields, and examine nonlinear six-component (C) wavefield characteristics through numerical simulations of~~ three fundamental ~~seismic~~ moment tensor sources~~.~~, exploring how geometric nonlinearity leads to body-wave coupling and energy redistribution, and its intrinsic dependence on the source type. Furthermore~~Additionally~~, using two moderate-to-strong earthquakes in the Taiwan region as examples, we explore the manifestation of nonlinear effects in a more complex scenario.~~we conduct theoretical simulations of focal mechanisms of near-field and strong earthquakes along the Taiwan coast, analyzing source-dependent nonlinear responses to establish foundational insights for guiding future observational data studies.~~

2 Theory and method

2.1 Elastodynamic theory

Consider a~~n~~ three-dimensional (3D) elastic medium in ~~three-dimensional space under~~an orthogonal Cartesian coordinate system (Fig. 1). ~~Let~~ An infinitesimal line element connecting a particle A at position **x** and~~within the medium, with~~ an adjacent

particle B at **x**+d**x**~~. The infinitesimal line element connecting these particles~~ has an initial length of ds. When subjected to external force, thi~~s~~e ~~material~~ element ~~AB~~ undergoes a displacement $\boldsymbol{u}(\boldsymbol{x}, t)$, moving ~~transitioning~~ to new positions A' and B' at **x**' and **x**'+d**x**', respectively, with a deformed length of ds'. This process includes~~deformation comprises~~ both rigid-body displacement and strain-induced distortion. ~~The work performed by the external force manifests as kinetic energy from particle motion and potential energy stored through elastic deformation.~~ The strain energy density can be characterized ~~quantified~~ by the ~~differential~~ quadratic form of the change in the ~~line~~ element's length, as shown ~~variation given~~ in Eq. (1).

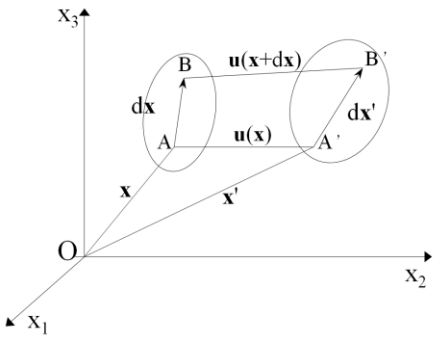

Figure 1. Schematic diagram of displacement and deformation of an infinitesimal line element in an elastic medium (a~~A~~dapted from Aki and Richards (2002))

$$(ds')^2 - (ds)^2 = 2E_{ij}dx_i dx_j, \ i, j \in \{1,2,3\} \tag{1}$$

where E_{ij} is ~~denotes~~ the Green-Lagrange strain tensor~~ components. All tensor equations adhere to the Einstein summation convention with dummy index notation. The displacement field u_i in Cartesian coordinate x_j defines the Green strain tensor (Eq. (2))~~, which provides an objective measure of deformation~~ ~~before and after external force application~~. In Cartesian coordinates, E_{ij} is defined by the displacement field as:

$$E_{ij} = \frac{1}{2}\left(\frac{\partial u_j}{\partial x_i} + \frac{\partial u_i}{\partial x_j} + \frac{\partial u_k}{\partial x_i} \cdot \frac{\partial u_k}{\partial x_j}\right), \ i, j, k \in \{1,2,3\} \tag{2}$$

The displacement gradient tensor can be decomposeds into a symmetric strain tensor (e_{ij}) and an antisymmetric rotation tensor (r_{ij}) components:

$$\frac{\partial u_j}{\partial x_i} = e_{ij} + r_{ij} \tag{3}$$

where,

$$e_{ij} = \frac{1}{2}\left(\frac{\partial u_j}{\partial x_i} + \frac{\partial u_i}{\partial x_j}\right), \quad r_{ij} = \frac{1}{2}\left(\frac{\partial u_i}{\partial x_j} - \frac{\partial u_j}{\partial x_i}\right) \tag{4}$$

Traditional linear elasticityConventional elastodynamic simplifies the problemtheory linearizes the Green strain tensor by neglecting the second-order product of displacement gradients in Eq. (2)terms ($\partial u_k/x_i \cdot \partial u_k/x_j$), thus reducing it to the Green-Lagrange strain tensor to the strain tensor e_{ij}:infinitesimal strain approximation:

$$E_{ij} \approx e_{ij} = \frac{1}{2}\left(\frac{\partial u_j}{\partial x_i} + \frac{\partial u_i}{\partial x_j}\right) \tag{5}$$

For an isotropic elastic mediummaterials, the stress-strain constitutivestrain-stress relationship is linear (generalized Hooke's law), given by Eq. (6), where λ and μ are the Lamé constants.given by:

$$\sigma_{ij} = \lambda \delta_{ij} e_{kk} + 2\mu e_{ij} \tag{6}$$

The theoretical framework of this study consistently employs the linear constitutive relationship described by Eq. (6). However, the complete Green-Lagrange strain tensor E_{ij} (rather than its linear approximation e_{ij}) is substituted into it, yielding a stress expression that reflects geometric nonlinearity: where λ and μ are Lamé coefficients, and δ_{ij} is the Kronecker delta. Incorporating nonlinearity through the complete Green strain tensor yields:

$$\sigma_{ij} = \lambda\delta_{ij}e_{kk} + 2\mu e_{ij} + \underbrace{\frac{1}{2}\lambda\delta_{ij}\left(\frac{\partial u_k}{\partial x_m}\cdot\frac{\partial u_k}{\partial x_m}\right) + \mu\frac{\partial u_k}{\partial x_i}\cdot\frac{\partial u_k}{\partial x_j}}_{\text{additional terms}},\ i,j,k,m\in\{1,2,3\} \tag{7}$$

Substituting this stress expression~~the nonlinear constitutive relation (Eq. (7))~~ into the momentum conservation law (Eq. (8)), ~~where ρ is the material density.~~

$$\rho\frac{\partial^2 u_i}{\partial t^2} = \frac{\partial \sigma_{ij}}{\partial x_j} \tag{8}$$

where ρ is the medium density, we finally obtain the nonlinear wave equation:~~Yields the nonlinear wave equation:~~

$$\rho\frac{\partial^2 u_i}{\partial t^2} = \underbrace{(\lambda+\mu)\frac{\partial^2 u_j}{\partial x_i\partial x_j} + \mu\frac{\partial^2 u_i}{\partial x_j\partial x_j}}_{\text{original terms}} + \underbrace{\lambda\frac{\partial u_k}{\partial x_i}\frac{\partial^2 u_k}{\partial x_j x_j} + \mu\left(\frac{\partial^2 u_k}{\partial x_i x_j}\cdot\frac{\partial u_k}{\partial x_j} + \frac{\partial^2 u_k}{\partial x_j x_j}\cdot\frac{\partial u_k}{\partial x_i}\right)}_{\text{additional terms}},\ i,j,k\in\{1,2,3\} \tag{9}$$

In Eq. (9), under the small-strain assumption, the original terms constitute ~~correspond to~~ the classic~~al~~ ~~linear~~ wave equation, while the subsequent additional terms arise from the geometric nonlinearity of strain~~nonlinear strain contributions~~. T~~T~~h~~ei~~se additional terms mathematically act as endogenous, secondary body force sources that depend on the wavefield itself.~~reveals two fundamental nonlinear effects:~~ In linear theory, P-waves (driven by the divergence field, representing volume change) and S-waves (driven by the curl field, representing shape change) are strictly decoupled. However, the existence of these nonlinear terms disrupts this decoupling. Specifically, the term $\partial u_k/\partial x_i \cdot \partial u_k/\partial x_j$ is a product of displacement gradients (which include both strain and rotation). When the P-wave (dominated by compressional strain) propagates, its non-uniform strain field generates spatial gradients. Through these higher-order terms, the gradient field of the P-wave can generate an equivalent

body force source with a curl component within the medium, which in turn radiates S-waves. The reverse is also true. This is the fundamental physical mechanism of P-S mode conversion: energy is transferred between the compressional and shear modes through the self-interaction of the wavefield.~~(i) Volumetric nonlinearity (associated with λ): Coupling between shear deformation and volumetric strain. (ii) Shear nonlinearity (associated with μ): Interdependence of shear stress and principal strains. These additional third-order terms introduce complex interactions between deformation modes that are absent in linear theory. Their seismic manifestations depend critically on material properties and source characteristics, necessitating targeted numerical simulations to quantify nonlinear effects on wave propagation.~~

2.2 Staggered-grid finite-difference method

To solve the nonlinear wave equation (9), we employ a high-accuracy Staggered-Grid Finite-Difference (SGFD) method~~The staggered-grid finite-difference (SGFD) technique has proven effective for simulating seismic wave propagation. This method employs dual grid systems to discretize velocity-stress formulations, enabling stable computation of wavefield evolution in discrete spatial-temporal domains~~ (Virieux, 1986;~~Madariaga, 1976;~~ Sun et al., 2018). First, by taking the time derivative of the nonlinear constitutive relation (7) and combining it with the momentum conservation equation (8), we convert the second-order wave equation into a system of first-order velocity-stress partial differential equations. This system includes additional stress-rate terms generated by the second-order products of displacement gradients. These terms update the displacement field through time integration of the

velocity field, thereby implementing the nonlinear coupling. The resulting velocity-stress equations are:

$$\begin{cases} \rho \dfrac{\partial v_i}{\partial t} = \dfrac{\partial \sigma_{ij}}{\partial x_j} \\ \dfrac{\partial \sigma_{ij}}{\partial t} = \lambda \delta_{ij} \dfrac{\partial E_{kk}}{\partial t} + 2\mu \dfrac{\partial E_{ij}}{\partial t} \\ \quad = \lambda \delta_{ij} \dfrac{\partial v_k}{\partial x_k} + \mu \left(\dfrac{\partial v_i}{\partial x_j} + \dfrac{\partial v_j}{\partial x_i} \right) + \underbrace{\lambda \delta_{ij} \left(\dfrac{\partial v_k}{\partial x_m} \cdot \dfrac{\partial u_k}{\partial x_m} \right) + 2\mu \dfrac{\partial v_k}{\partial x_i} \cdot \dfrac{\partial u_k}{\partial x_j}}_{\text{additional terms}} \end{cases}, \quad i, j, k, m \in \{x, y, z\} \tag{10}$$

where $v_i = \partial u_i / \partial t$. In the SGFD scheme, different physical quantities are staggered on the spatial grid cells. This arrangement naturally satisfies the central-difference approximation for differential operators, effectively suppressing numerical dispersion and enhancing computational stability and accuracy, as illustrated in Fig. 2~~, stress and velocity components are distributed across offset grid points to optimize numerical accuracy~~.

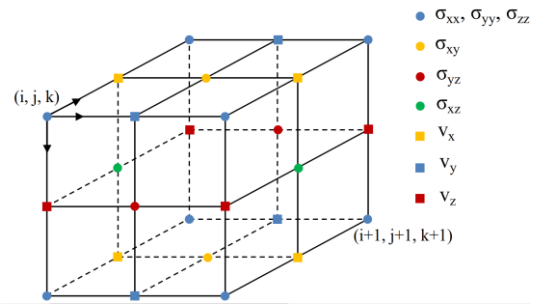

Figure 2. 3D staggered-grid configuration for velocity-stress formulations, showing the placement of velocity components and stress components.

To handle the model's truncated boundaries, ~~For 3D elastic isotropic media, we extend conventional linear strain formulations (Pei, 2005) by incorporating the nonlinear strain tensor E_{ij}. Temporal differentiation of the constitutive relation(Eq.(7))~~

yields velocity-stress relationships when combined with Eq. (8).

$$\begin{cases} \rho \dfrac{\partial v_i}{\partial t} = \dfrac{\partial \sigma_{ij}}{\partial x_j} \\ \dfrac{\partial \sigma_{ij}}{\partial t} = \lambda \delta_{ij} \dfrac{\partial E_{kk}}{\partial t} + 2\mu \dfrac{\partial E_{ij}}{\partial t} \\ \quad = \lambda \delta_{ij} \dfrac{\partial v_k}{\partial x_k} + \mu \left(\dfrac{\partial v_i}{\partial x_j} + \dfrac{\partial v_j}{\partial x_i} \right) + \underbrace{\lambda \delta_{ij} \left(\dfrac{\partial v_k}{\partial x_m} \cdot \dfrac{\partial u_k}{\partial x_m} \right) + 2\mu \dfrac{\partial v_k}{\partial x_i} \cdot \dfrac{\partial u_k}{\partial x_j}}_{\text{additional terms}} \end{cases} , \; i, j, k, m \in \{1, 2, 3\} \quad (10)$$

where $v_i = \partial u_i / \partial t (i \in \{x, y, z\})$. Nonlinear contributions emerge through velocity-displacement coupling, whereupon take the displacement-preserving terms (u_i) as products of velocity components v_i and time dt (serve as time step in simulations) in the equations. In addition, rotation rates around Cartesian axes are derived from the antisymmetric rotation tensor (Eq. (4)).

Based on the equations, we implement these formulations through C/C++ code to numerically simulate seismic wave propagation. It containswe employ the perfectly Perfectly matched Matched layer Layer (PML) absorbing boundary to suppress boundary reflectionscondition (Dong and Ma, 2000Li et al., 2015). For simulations involving a free surface, and acoustic boundary replacement (Eq. (13)) forthe free-surface boundary is implementedation at the top of the model by setting the acoustic boundary replacement (Xu et al., 2007; Wang et al., 2012). The numerical code used in this study has been benchmarked against international standard programs, including SPICE/SISMOWINE and SPECFEM2D. The comparison is provided in the supplementary material.

32.31 Source implementation and simulation Forward modelling parameters

The sSeismic moment tensors M_{ij} provideis the most-complete mathematical

representation of an equivalent body-force system for a point sources (Gilbert, 1970). ~~when the seismic wavelength exceeds the source dimension (Gilbert, 1970). As defined in Eq. (12), the symmetric second-order moment tensor **M** quantifies the equivalent force system acting at the hypocenter:~~

~~$$M_{ij} = \mu A(v_i n_j + v_j n_i),\ i,j \in \{1,2,3\} \quad (12)$$~~

~~Where μ is the shear modulus, A the fault area, v_i the slip vector, and n_i the fault normal vector. The tensor~~It can be decomposed into three fundamental components: isotropy (ISO) ~~component~~, double couple (DC) ~~component~~, and compensated linear vector dipole (CLVD) ~~component~~ (Knopoff and Randall, 1970; Jost and Hermann, 1989). ~~Specifically, the ISO component represents volumetric change with non-zero trace and uniform force along principal axes. The DC component signifies pure shear dislocation without volumetric change without volume variation. The CLVD component describes axial contraction/expansion with a dipole magnitude ratio 2:−1:−1.~~ These moment tensor expressions can be written as Eq. (11~~3~~). ~~These components govern distinct radiation patterns critical for understanding nonlinear seismic wave propagation effects.~~

$$\boldsymbol{M}^{ISO} = \begin{pmatrix} M_{xx} & 0 & 0 \\ 0 & M_{yy} & 0 \\ 0 & 0 & M_{zz} \end{pmatrix}, \boldsymbol{M}^{DC} = \begin{pmatrix} 0 & M_{xy} & 0 \\ M_{yx} & 0 & 0 \\ 0 & 0 & 0 \end{pmatrix}, \boldsymbol{M}^{CLVD} = \begin{pmatrix} M_{xx} & 0 & 0 \\ 0 & M_{yy} & 0 \\ 0 & 0 & -2M_{zz} \end{pmatrix} \quad (13\text{~~3~~}1)$$

In our SGFD framework, we follow the method proposed by Graves (1996) to implement the moment tensor source by converting the moment rate tensor into equivalent body forces. The equivalent velocity increment Δv^n added on the grid can be expressed as: ~~Following Graves(1996), we implement moment tensor sources in the staggered-grid finite-difference scheme by converting body force to equivalent~~

velocity sources. The loading equations for the three moment sources are shown in Eq. (14).

$$\boldsymbol{M}^{ISO}:\ \Delta v_i^n = \frac{M_{ij}\cdot dt\cdot f^n}{\rho V}\cdot\frac{\partial}{\partial x_j}$$

$$\boldsymbol{M}^{DC}:\ \Delta v_i^n = \frac{M_{jk}\cdot dt\cdot f^n}{\rho V}\cdot(\delta_{ij}\frac{\partial}{\partial x_k}+\delta_{ik}\frac{\partial}{\partial x_j}) \qquad (124)$$

$$\boldsymbol{M}^{CLVD}:\ \Delta v_i^n = \frac{M_{kl}\cdot dt\cdot f^n}{\rho V}\cdot(\delta_{ik}\frac{\partial}{\partial x_l}+\delta_{il}\frac{\partial}{\partial x_k}-\frac{2}{3}\delta_{kl}\frac{\partial}{\partial x_i})$$

where $i, j, k, l \in \{1x, 2y, 3z\}$. Δv denotesis the velocity increment, n is the time--step index, dt is the time stepinterval, ρ is the material density, and V is the grid cell volume. The source-time function, and f^n usesis the value of the source-time function at time n·dt.a Ricker wavelet with amplitude at $n \cdot dt$.

WTo exclude effects on nonlinear wave propagation from complex medium characteristics, we econductcurrently focus exclusively on simulations in a 3D homogeneous, isotropic, 3D full-space model to isolate the effects of nonlinearity from those of complex media. The model parameters are: P-wave velocity v_p=4400 m/s, S-wave velocity v_s=3000 m/s, and density ρ=2600 kg/m^3. numerical implementation employs the Ricker wavelet with a 0.5 Hz dominant frequency. The model spansspace is 8014 km (x) × 8014 km (y)× 8014 km, (z) with a uniform grid spacing of $\Delta x = \Delta y = \Delta z = 50$ m500 meters in X, Y, and Z directions. Material properties are: P-wave velocity v_p=4400 m/s, S-wave velocity v_s=3000 m/s, and density ρ=2600 kg/m^3. The source residesis located at the model center (40 km, 40 km, 40 km). It uses a Ricker wavelet with a dominant frequency of 4 Hz as the source-time function. Receivers are arranged on a spherical surface with a radius of 5 km centered at the source to sample wavefields at various azimuths. The time step

285 is~~Temporal discretization uses Δt = 15 m~~0.0015s.~~, with second-order differential~~

286 ~~accuracy in time and sixth-order in space.~~

287 ~~For Numerical stability, based on the simulation parameters, the spatial~~

288 ~~discretization achieves 10.4 ($v_s/\Delta/f_{dominant}$) points per wavelength for the dominant~~

289 ~~frequency, which exceeds the 8–10 PPW threshold for sixth-order schemes to~~

290 ~~suppress numerical dispersion artifacts (Virieux, 1986). Follows the temporal stability~~

291 ~~of 3D Courant–Friedrichs–Lewy (CFL) criterion ($\Delta t \cdot v_{max} \cdot \mathrm{sqrt}(1/\Delta x^2+1/\Delta y^2+1/\Delta z^2)$), it~~

292 ~~reaches about 0.16. The resultant CFL number is a conservative value relative to the~~

293 ~~empirical 3D stability limit of 0.5 (Moczo et al., 2007), ensuring waveform fidelity~~

294 ~~while accommodating potential nonlinear term amplification~~

295 The shortest wavelength for the 4 Hz dominant frequency is the S-wavelength

296 (λ_S = 750 m). Based on the 50 m grid spacing, there are 15 grid points per wavelength,

297 which is well above the threshold required for high-order finite-difference schemes

298 (Virieux, 1986). The Courant-Friedrichs-Lewy (CFL) number is approximately 0.23,

299 which is well below the stability limit for 3D finite-difference methods (Moczo et al.,

300 2007), ensuring the stability and accuracy of the numerical computation.

301 ~~3.2 Simulation results~~

302

303 $$\begin{cases} \sigma^0_{zz} = 0 \\ \rho = 0.5\rho_0 \\ \lambda = 0 \\ \mu = \mu_0 \end{cases} \quad (11)$$

304 ~~where σ^0_{zz}, ρ, λ, and μ denote normal stress, medium density, and Lamé coefficients at~~

305 ~~and above the free surface, while ρ_0 and μ_0 represent density and Lamé coefficients~~

~~below the free surface, respectively.~~

3 Comparison of s~~S~~imulation~~s of basic seismic moment sources~~ results

~~3.1 Forward modelling parameters~~

~~Seismic moment tensors provide the most complete mathematical representation of point sources when the seismic wavelength exceeds the source dimension (Gilbert, 1970). As defined in Eq. (12), the symmetric second-order moment tensor **M** quantifies the equivalent force system acting at the hypocenter:~~

$$M_{ij} = \mu A(v_i n_j + v_j n_i),\ i,j \in \{1,2,3\} \quad (12)$$

~~Where μ is the shear modulus, A the fault area, v_i the slip vector, and n_j the fault normal vector. The tensor can be decomposed into three fundamental components: isotropy (ISO) component, double couple (DC) component, and compensated linear vector dipole (CLVD) component (Knopoff and Randall, 1970; Jost and Hermann, 1989). Specifically, the ISO component represents volumetric change with non-zero trace and uniform force along principal axes. The DC component signifies pure shear dislocation without volumetric change without volume variation. The CLVD component describes axial contraction/expansion with a dipole magnitude ratio 2:−1:−1. These moment tensor expressions can be written as Eq. (13). These components govern distinct radiation patterns critical for understanding nonlinear seismic wave propagation effects.~~

$$\boldsymbol{M}^{ISO} = \begin{pmatrix} M_{11} & 0 & 0 \\ 0 & M_{22} & 0 \\ 0 & 0 & M_{33} \end{pmatrix}, \boldsymbol{M}^{DC} = \begin{pmatrix} 0 & M_{12} & 0 \\ M_{21} & 0 & 0 \\ 0 & 0 & 0 \end{pmatrix}, \boldsymbol{M}^{CLVD} = \begin{pmatrix} M_{11} & 0 & 0 \\ 0 & M_{22} & 0 \\ 0 & 0 & -2M_{33} \end{pmatrix} \quad (13)$$

~~Following Graves(1996), we implement moment tensor sources in the~~

~~staggered-grid finite-difference scheme by converting body force to equivalent velocity sources. The loading equations for the three moment sources are shown in Eq. (14).~~

$$\boldsymbol{M}^{ISO}:\ \Delta v_i^n = \frac{M_{ij}\cdot dt\cdot f^n}{\rho V}\cdot\frac{\partial}{\partial x_j}$$

$$\boldsymbol{M}^{DC}:\ \Delta v_i^n = \frac{M_{jk}\cdot dt\cdot f^n}{\rho V}\cdot(\delta_{ij}\frac{\partial}{\partial x_k}+\delta_{ik}\frac{\partial}{\partial x_j}) \qquad (14)$$

$$\boldsymbol{M}^{CLVD}:\ \Delta v_i^n = \frac{M_{kl}\cdot dt\cdot f^n}{\rho V}\cdot(\delta_{ik}\frac{\partial}{\partial x_l}+\delta_{il}\frac{\partial}{\partial x_k}-\frac{2}{3}\delta_{kl}\frac{\partial}{\partial x_i})$$

~~where $i, j, k, l\in\{1,2,3\}$. Δv denotes velocity increment, n the time step index, dt the time interval, ρ material density, and V grid cell volume. The source-time function f^n uses a Ricker wavelet with amplitude at $n\cdot dt$.~~

~~To exclude effects on nonlinear wave propagation from complex medium characteristics, we currently focus exclusively on simulations in a 3D homogeneous isotropic full-space model. The numerical implementation employs the Ricker wavelet with a 0.5 Hz dominant frequency. The model spans 80 km (x) × 80 km (y)× 80 km (z) with a uniform grid spacing of 500 meters in X, Y, and Z directions. Material properties are: P-wave velocity v_p=4400 m/s, S-wave velocity v_s=3000 m/s, and density ρ=2600 kg/m^3. The source resides at the model center (40 km, 40 km, 40 km). Temporal discretization uses Δt = 15 ms, with second-order differential accuracy in time and sixth-order in space.~~

~~For Numerical stability, based on the simulation parameters, the spatial discretization achieves 10.4 ($v_s/\Delta/f_{dominant}$) points per wavelength for the dominant frequency, which exceeds the 8–10 PPW threshold for sixth-order schemes to suppress numerical dispersion artifacts (Virieux, 1986). Follows the temporal stability~~

~~of 3D Courant-Friedrichs-Lewy (CFL) criterion ($\Delta t \cdot v_{max} \cdot \sqrt{1/\Delta x^2 + 1/\Delta y^2 + 1/\Delta z^2}$)), it reaches about 0.16. The resultant CFL number is a conservative value relative to the empirical 3D stability limit of 0.5 (Moczo et al., 2007), ensuring waveform fidelity while accommodating potential nonlinear term amplification.~~

~~3.2 Simulation results~~

3.1 Basic characteristics of nonlinear seismic wavefields

~~3.2.1 ISO source~~

Fig. 3(a) displays the 6C wavefield snapshots ~~at 8 seconds~~ for the ISO source at t=1.5s~~under nonlinear deformation condition. Translational components exhibit uniform P-wave amplitudes~~, while Fig. 3(b) compares the linear and nonlinear waveforms recorded at a specific receiver~~rotational components show near absence of P-wave energy~~. Within the framework of linear~~The wavefield differences between linear and nonlinear simulations (Fig.3b) reveal emergent S-wave signatures, contrasting with classical elastodynamic~~ theory, an ~~where~~ ISO source~~s exclusively~~ only generates P-waves in homogeneous elastic ~~isotropic~~ media~~ through pure compressional/expansional volume change~~. However, a faint signal is still recorded in the P-wave window of the rotational components in the linear simulation (black line). This signal originates from the spatial gradients produced by the wavefront curvature of the near-field P-wave. In the far field, P-wavea can be approximated as an irrotational plane wave with no curl in its displacement field. In the near field, however, the spatial gradients of its displacement field can generate weak rotation.

This signal is very weak compared to the rotational signals generated by S-waves, and is therefore treated in this study as the baseline background for assessing the nonlinear contributions.

The waveform comparison shows that in the S-wave window, the nonlinear simulation exhibits a distinct response with obvious amplitude, whereas the linear simulation is near zero in the ISO results. This vibration is attributed to the P-to-S mode conversion of energy, caused by geometric nonlinearity. Analysis of the waveform characteristics in Fig. 3(b) reveals that the EM caused by nonlinearity is larger in the rotational components than in the translational ones, while the PM is nearly zero. This indicates that the primary effect of geometric nonlinearity is to modulate the energy distribution and envelope shape of the waves, rather than perturbing their propagation velocity or arrival time. This effect originates from the higher-order nonlinear terms in the strain-displacement relationship. These terms act as new, endogenous body force terms in the wave equation, equivalent to producing minor secondary perturbations in the wave's propagation. These perturbations interact with the primary wavefield, thereby reallocating energy and ultimately altering the wave's amplitude and shape. For instance, as a P-wave from an ISO source propagates, its non-uniform strain field generates spatial gradients. Through the self-interaction of these gradients via the nonlinear terms, an equivalent body force source with a curl component is generated within the medium, which then radiates S-waves.

~~The anomalous P-S coupling phenomenon arises from nonlinear~~

~~volumetric-shear strain interactions governed by the constitutive relationship (Eq. (7)),~~ ~~where the higher-order terms enable energy transfer between compressional and shear deformation modes.~~

~~Fig. 4 quantified the relative change between linear and nonlinear simulations at each grid cell volume. We applied a stability threshold to the relative change calculations to mitigate the influence of unrealistic wavefields ($value_{linear} \rightarrow 0$). It can be seen from Fig.4 that (i) the spatial distribution exhibits general symmetry and homogeneity with alternating positive/negative anomalies (Fig. 4a), where negative values (<0) indicate overestimation by linear theory and positive values (>0) suggest underestimation; (ii) rotational components have different and more complex azimuthal distribution and larger relative changes than translational components, also evidenced by probability density function (PDF) distributions in (Fig. 4b).~~

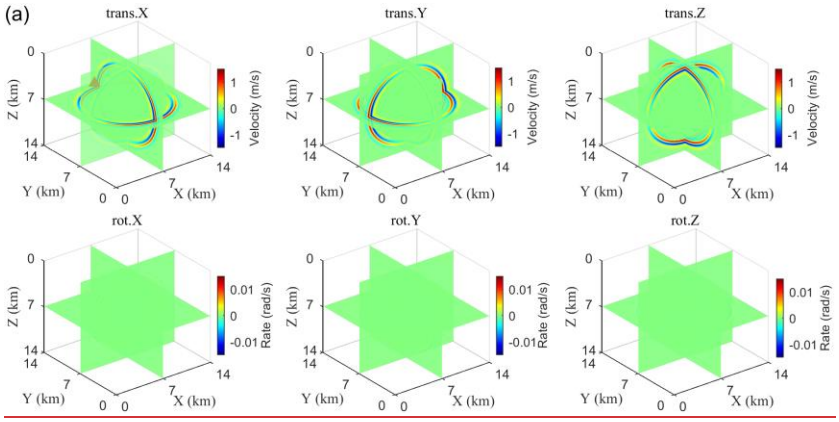

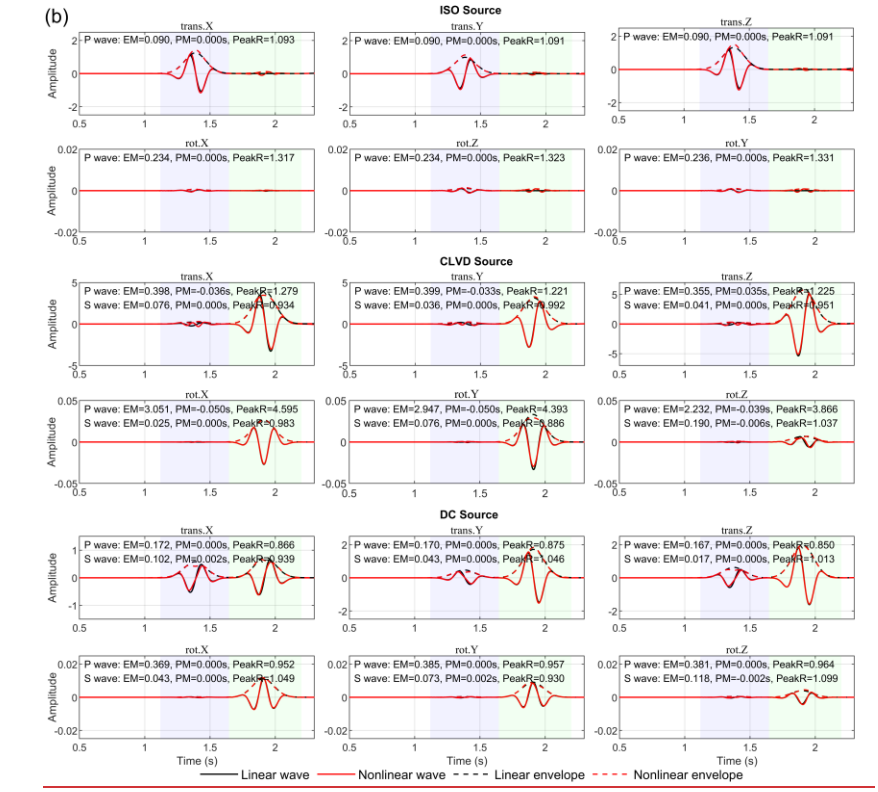

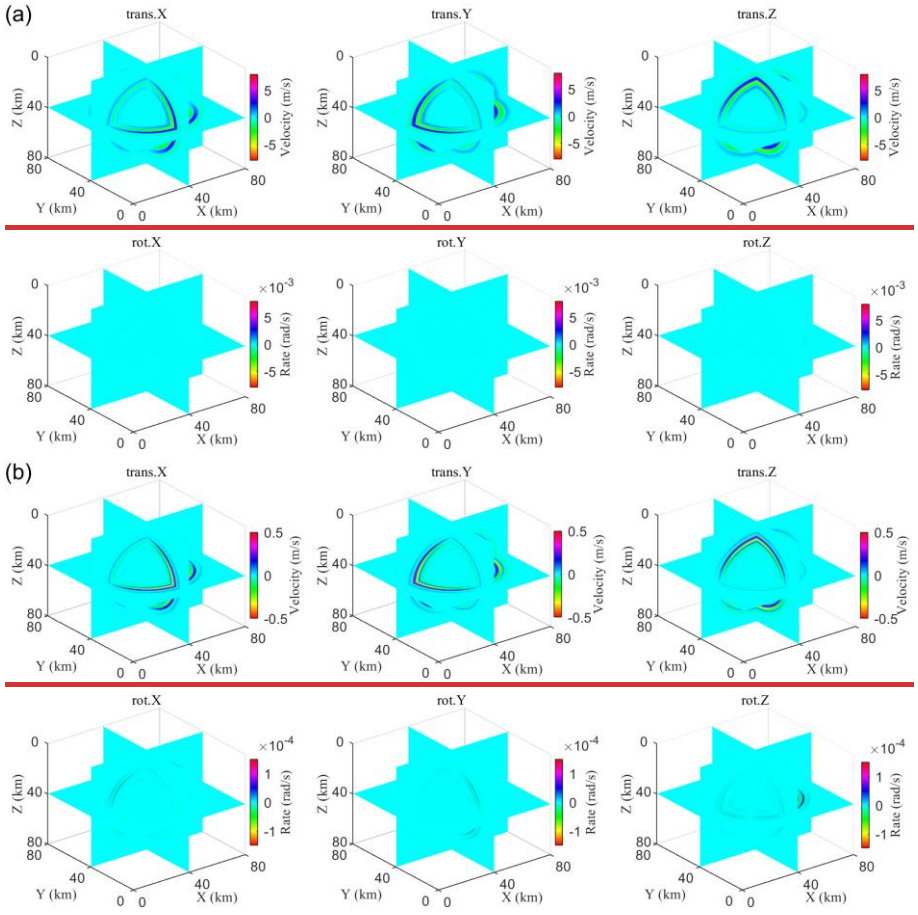

Figure 3. (a) Snapshot of the 6C wavefield from the linear ISO source simulation and the location of the example receiver (indicated by the red triangle on the trans.X

component). (b) Comparison of the waveforms and envelope characteristics of the linear and nonlinear simulations at this receiver. The P-wave and S-wave analysis windows are marked. EM: envelope misfit; PM: phase misfit; PeakR: Peak ratio.~~(a) Nonlinear 6C wavefield and (b) linear-nonlinear discrepancy for Mw7 ISO source at t=8s.~~

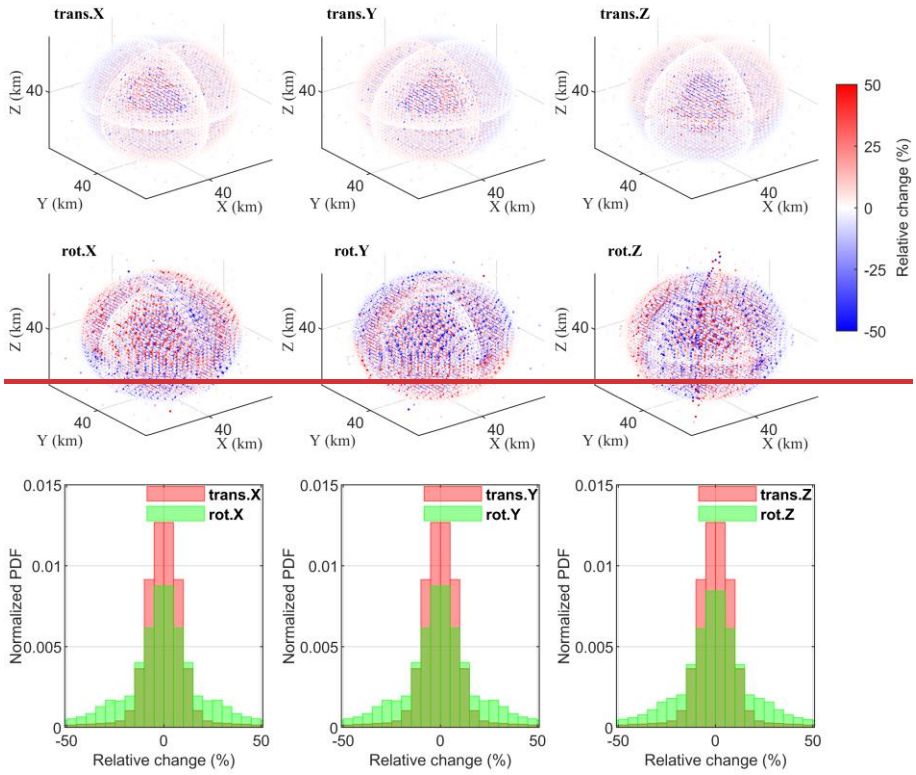

~~**Figure 4.** ISO source linear-nonlinear relative change: (a) 3D spatial distribution (b) Probability density function.~~

~~3.2.2 DC source~~

We next calculated the energy of the residual waveforms between the linear and nonlinear simulations. Fig. 4 shows the projection of this metric in the P-wave and S-wave windows onto three principal planes.

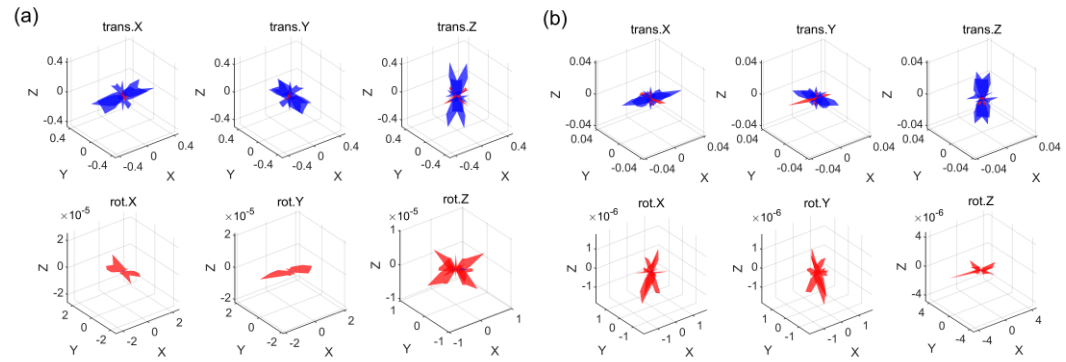

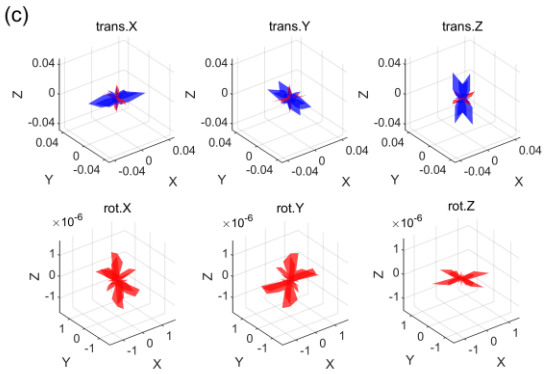

Figure 4. 3D spatial projection of the intensity of waveform perturbations generated by nonlinearity. (a)-(c) are the results for CLVD, DC, and ISO sources, respectively. Each subplot shows the projection of the nonlinear effect intensity of the P-wave (blue) and the S-wave (red).

The results indicate that the radiation of the nonlinear effect follows fundamental wave physics principles. In the translational components, the nonlinear effect of the P-wave is much stronger than that of the S-wave, and its dominant direction is consistent with the corresponding coordinate axes, reflecting the direction of the strongest strain gradient in the linear P-wave field. Consequently, the nonlinear effect is strongest in the direction where the theoretical linear P-wave amplitude projects most strongly onto the corresponding Cartesian component (e.g., the X-axis direction for the trans.X component). In the rotational components, the nonlinear perturbation

in the S-wave is dominant. This is because rotational motion is generated by shear strain gradients, and the S-wave, carrying substantial shear energy, is most effective at producing the shear strain gradients required to drive rotation.

Building on the time-domain analysis, spectral analysis was conducted on waveforms in the P- and S-wave windows of the median and interquartile range (IQR) of the Power Spectral Density (PSD), as shown in Fig. 5. For the CLVD and DC sources, the median nonlinear spectrum is systematically higher than the median linear spectrum in the mid-to-high frequency band (approx. 5-20 Hz) in both P- and S-waves, and this phenomenon is more pronounced in the rotational components. The translational component spectra are nearly identical in the ISO source simulation. In the S-wave comparison for the ISO source, the linear translational and rotational energies are extremely low, essentially at the level of numerical simulation noise. In contrast, the nonlinear spectrum is several orders of magnitude higher, providing frequency-domain evidence for the nonlinear P-S mode conversion. The IQR of the PSD indicates that the nonlinear effects exhibit strong spatial variability, being enhanced in some azimuths while potentially being weakened in others, thus showing significant azimuthal dependence. The spectral comparison reveals a key feature of the nonlinear effect: energy transfer to higher frequencies. The energy injected by the source, primarily concentrated at lower frequencies, is efficiently pumped by the nonlinear secondary source and re-radiated as higher-frequency energy. This redistribution of high-frequency energy, accompanied by the mode conversion of P- and S-waves, collectively causes the nonlinear spectral lines to be systematically

higher than the linear ones in the mid-to-high frequency range.

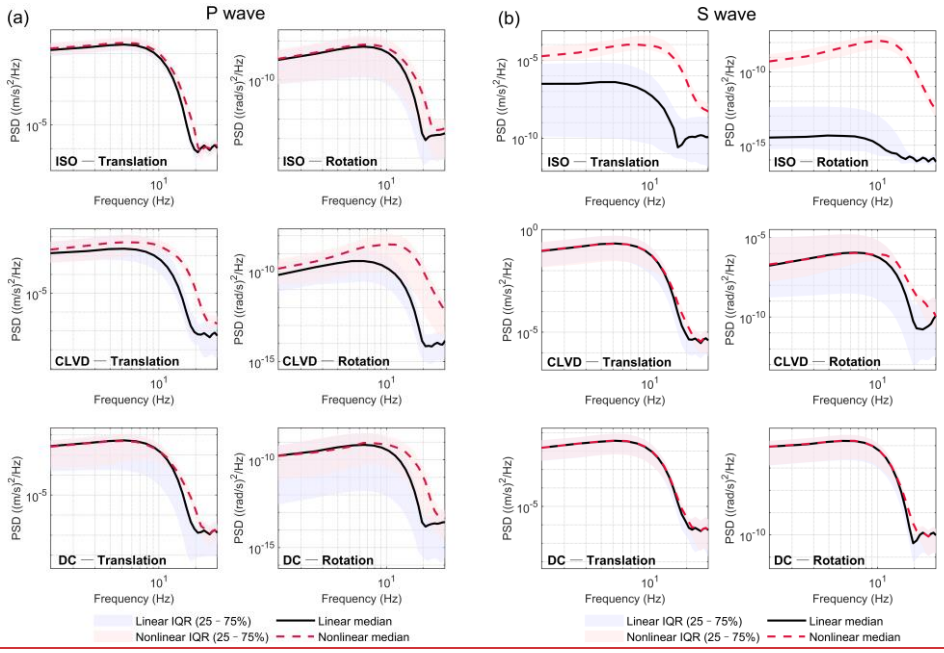

Figure 5. Comparison of the (a) P-wave and (b) S-wave PSD of translational and rotational components. The black solid line is the median PSD from the linear simulations, the red dashed line is from the nonlinear simulations, and the shaded area represents the 25%-75% IQR.~~Fig. 5a presents 6C wavefield snapshots for the DC source under nonlinear conditions. The wavefield difference between nonlinear and linear wavefields in Fig. 5b demonstrates a different wavefront energy distribution from the original wavefront distribution in Fig. 5a. This energy redistribution caused by nonlinearity indicates that shear-dominated sources induce more complex nonlinear interactions.~~

~~The relative changes of nonlinear effects (Fig. 6) reveal not only zone variation but also localized strong nonlinearities at axial positions related to the distribution of the force couples tied to the DC source of fault displacement directions. At the same time, rotational components show a similar spatial distribution of underestimated and~~

overestimated areas and localized strong nonlinearities, and rot.X and rot.Y components show larger change values, as seen from the PDF results.

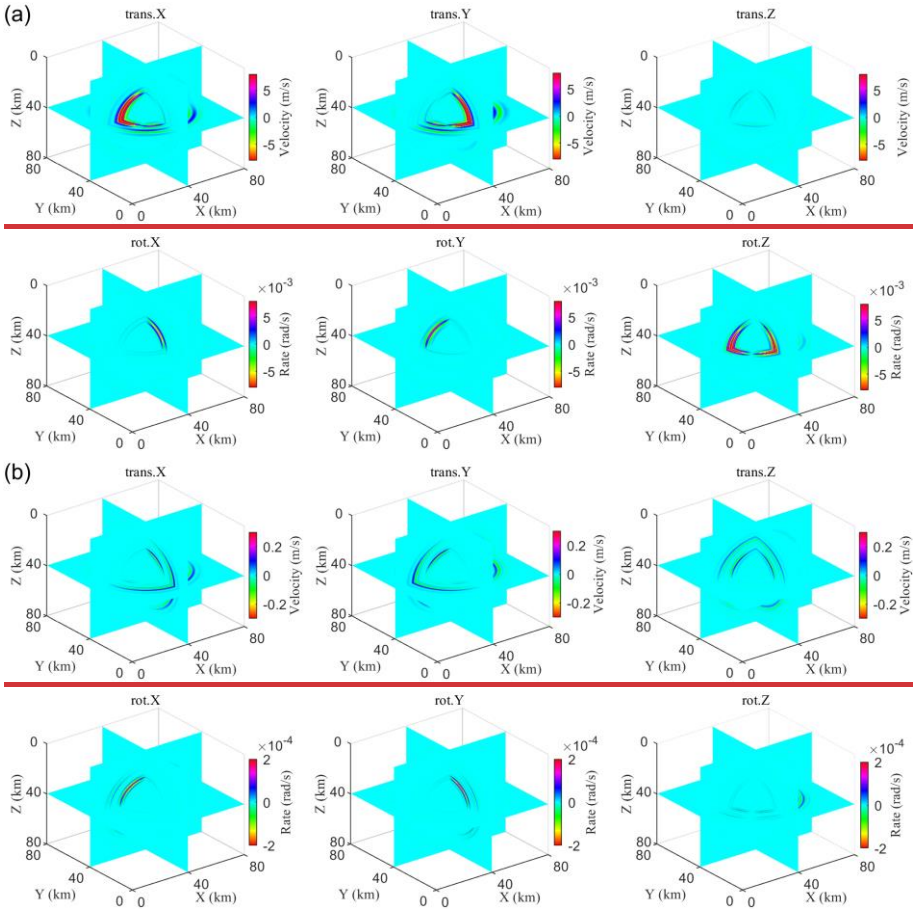

Figure 5. (a) Nonlinear 6C wavefield and (b) linear-nonlinear discrepancy for Mw7 DC source at t=8s.

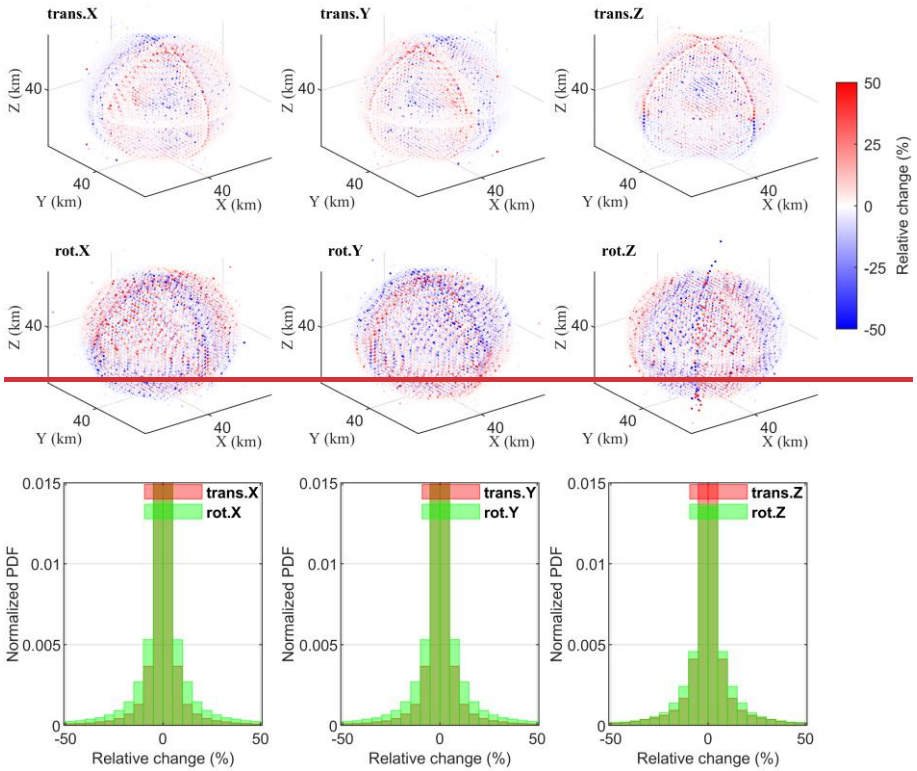

~~Figure 6.~~ ~~DC source linear-nonlinear relative change: (a) 3D spatial distribution (b) Probability density function.~~

3.1 Source-type dependency of nonlinear effects

~~3.2.3 CLVD source~~

Fig. 6 presents the log-ratio of nonlinear to linear energy ($\log(E_{nl} / E_{lin})$) for the tangential energy in the P-wave (E^P) and the radial energy in the S-wave (E^S). The energy E is obtained by time-integrating the square of the wavefield amplitude. Fig. 6, through scatter plots and statistics, shows the distribution of the logarithmic energy ratios for the three source types, quantitatively assessing the overall impact of nonlinear effects on the energy of specific wave types.

Regarding the tangential energy in the P-wave (Fig. 6(a)), the nonlinear

enhancement is most significant for the CLVD source, followed by the DC source, while the effect of the ISO source is minimal. This indicates that the CLVD source is the most effective mechanism for exciting the nonlinear growth of P-wave tangential energy. For the radial energy in the S-wave (Fig. 6(b)), the net effect of nonlinearity for the CLVD and DC sources is not statistically significant, possibly due to the cancellation of azimuthal enhancement and reduction.

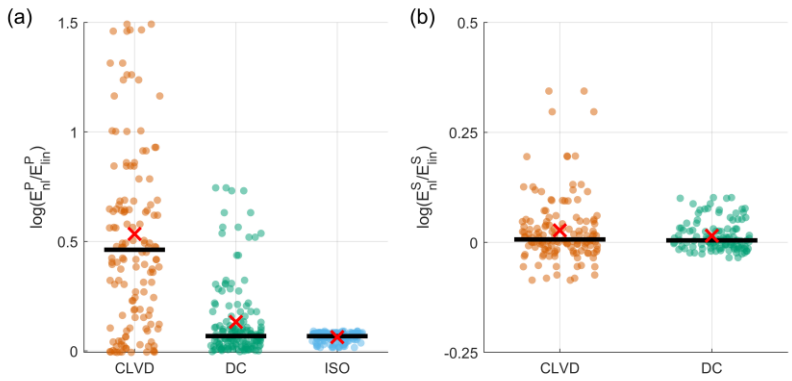

Figure 6. Distribution of the nonlinear/linear log-ratio for (a) tangential energy in the P-wave and (b) radial energy in the S-wave. The dots represent the values for each independent receiver; the black bar indicates the median of the data; the red cross indicates the arithmetic mean.

To further investigate the impact of nonlinearity on the micro-properties of the wavefield, we introduce two quantitative metrics to analyze the waveform attribute changes within the P-wave window. First, we use rectilinearity (rect) to measure the deviation of P-wave particle motion from a straight line. This metric is calculated based on the eigenvalues of the covariance matrix. The sign of the change, $\Delta rect = rect_{nl} - rect_{lin}$, reflects whether the nonlinearity promotes or suppresses the leakage of P-wave energy into the tangential direction. Second, to explore the coupling

relationship between different motion modes, we introduce the rotation-translation correlation (corr). This metric calculates the Spearman's rank correlation coefficient between the time series of the tangential velocity magnitude and the rotation rate magnitude, quantifying the synchrony of the time-varying intensity envelopes of these two physical motions.

Fig. 7(a) shows the statistical distribution of the differences in these two metrics. For all three sources, Δcorr is generally positive, indicating that geometric nonlinearity may be a common physical mechanism that enhances the coupling between rotation and translation. In contrast, the distribution of Δrect shows a pronounced source dependence: the ISO source causes weak changes, the DC source induces significant negative changes, while the CLVD source primarily causes positive changes. The spatial distribution of Δrect in Fig. 7(b) further reveals its essential connection to the source's strain state. For the ISO source, characterized by pure volumetric strain, the pure volumetric strain excites a very weak shear effect through nonlinearity, leading to a slight decrease in P-wave rectilinearity, but the efficiency of this conversion is extremely low. For the pure-shear DC source, the significant decrease in rectilinearity is concentrated near the P-wave radiation nodes, which are the regions with the strongest linear shear strain gradients. This indicates that in these regions, the efficiency of the nonlinear P-S mode conversion is highest, leading to a noticeable decrease in rectilinearity. For the CLVD source, which combines strong uniaxial compression and axisymmetric shear, the increase in rectilinearity is also concentrated in regions with strong strain gradients. The result

reveals that, in a complex stress state with coexisting tension and compression, the nonlinear effect may instead constrain energy to propagate in the radial direction, suppressing leakage into the tangential direction, thereby purifying the P-wave motion.

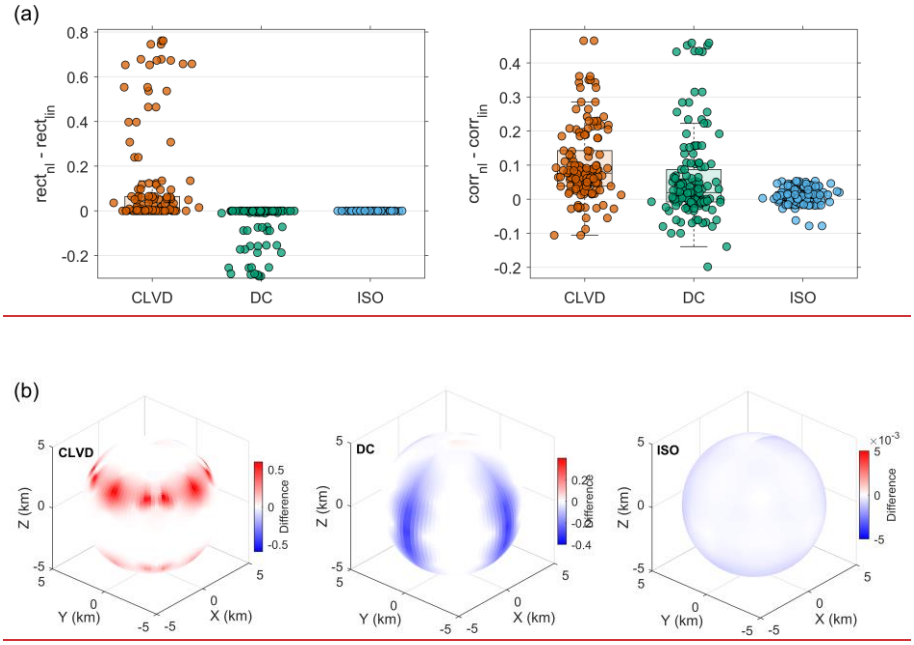

Figure 7. (a) Statistical distribution of the change in P-wave rectilinearity and rotation-translation correlation changes, and (b) spherical spatial distribution of Δrect in different receivers.

In summary, the analysis of the wavefield properties demonstrates that the manifestation of nonlinear effects is fundamentally controlled by the type of strain field initialized by the source and the geometry of its spatial gradients. Different source mechanisms, by initializing different strain fields, thus modulate the mode, intensity, and even the effect of the nonlinear response.

4 Simulation of nonlinear effects for referenced earthquake events~~Earthquakes simulations~~

To extend the understanding established in the idealized full-space model to more realistic scenarios involving complex propagation effects~~Building upon the theoretical framework for fundamental source types~~, we further ~~extend our~~ simulat~~eions~~ two moderate-to-strong referenced earthquakes that occurred in the coastal region of Taiwan: event~~more complex scenarios incorporating realistic source mechanisms and layered media. Analyzing two moderate-magnitude earthquakes (~~E1~~:~~ (Mw 5.4) and event E2~~:~~ (Mw6.1) along the Taiwan coast aims to validate theoretical predictions of nonlinear wave propagation and establish baseline understanding for future observational comparisons~~. The epicenters and ~~events were respectively recorded at~~ station locations of these two referenced events are ~~s NA01 (E1) and QS01 (E2) (Chen et al., 2023), as~~ shown in Fig. S~~-~~4~~10, depicted by GMT (Wessel et al., 2019). Moment tensor solutions derived from the U.S. Geological Survey (USGS) are defined in Eq. (16), with synthetic 6C seismograms generated under both linear and nonlinear constitutive relations.~~. Unlike the preceding basic source simulations, the models in this section employ a layered velocity structure based on the CRUST1.0 model (Laske et al., 2013) to approximate the real Earth's structure (see Table S5). The source mechanisms for both events (Eq. (13)) are mixed sources. Other detailed simulation parameters for the two referenced earthquake simulations are provided in Table S6.

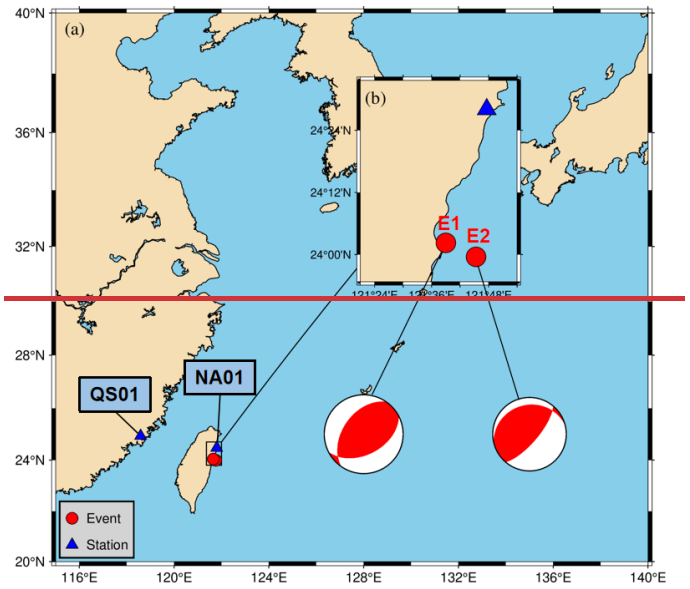

~~Figure 10.~~ ~~Epicenters and observation sites of E1 and E2~~

$$E1:\begin{bmatrix} M_{xx}=-7.569\times10^{16}, M_{yy}=-2.373\times10^{16}, M_{zz}=9.942\times10^{16} \\ M_{xz}=7.372\times10^{16}, M_{yz}=-1.0965\times10^{17}, M_{xy}=4.156\times10^{16} \end{bmatrix}$$
$$E2:\begin{bmatrix} M_{xx}=-1.064\times10^{18}, M_{yy}=-7.607\times10^{17}, M_{zz}=1.8247\times10^{18} \\ M_{xz}=3.141\times10^{17}, M_{yz}=3.155\times10^{17}, M_{xy}=1.114\times10^{18} \end{bmatrix} \quad (13\text{~~6~~})$$

Fig. 8 shows the results for the E1. Compare the waveforms and the time-frequency energy difference in Fig. 8(b). In the translational components, the energy changes induced by nonlinearity are relatively dispersed in different types of waves. However, most are concentrated during the arrival of S-wave (approx. 15-20 s) and the subsequent surface waves, and faint but persistent nonlinear perturbations are also observed during the P-wave and its subsequent multiple reflections/conversions (approx. 5-15 s). In the rotational components, the nonlinear response energy is more concentrated than in the translational components. Energy perturbations can be observed on the rot.T component before the direct S-wave arrival, which may correspond to nonlinear effects excited by S-waves converted from P-waves or S-waves reflected/transmitted within the layered medium. For the rot.R and rot.Z

components, the nonlinear effects are primarily associated with the arrival of the direct S-wave. Different components showing different extents of nonlinearity may stem from the azimuthal location of this receiver~~To isolate source-related nonlinearity, we simulate both earthquakes adopting the a simplified laterally homogeneous crustal model based on CRUST1.0 (Laske et al., 2013), with physical properties and simulation parameters listed in Tables 2 and 3. Free-surface condition is used at the top, and perfectly matched layer (PML) condition is used on other boundaries, with 10-order differential accuracy in space~~.

~~**Table 2.** Physical properties of layered media.~~

~~Layer~~	~~Thickness (km)~~	~~vp (km/s)~~	~~vs (km/s)~~	~~ρ (kg/m^3)~~
~~1~~	~~0.50~~	~~2.50~~	~~1.07~~	~~2.11~~
~~2~~	~~10.12~~	~~5.80~~	~~3.40~~	~~2.63~~
~~3~~	~~9.81~~	~~6.30~~	~~3.62~~	~~2.74~~
~~4~~	~~9.82~~	~~6.90~~	~~3.94~~	~~2.92~~
~~5~~	~~-~~	~~7.70~~	~~4.29~~	~~3.17~~

~~**Table 3** Simulation parameters~~

~~Iterm~~	~~Paremeter (E1, E2)~~
~~Dominant frequency~~	~~1 Hz, 0.5 Hz~~
~~Moment magnitude~~	~~Mw5.4, Mw6.1~~
~~Depth~~	~~15 km, 30 km~~
~~Grid spacing~~	~~1 km, 2 km~~
~~Time step~~	~~5 ms, 2 ms~~
~~Source mechanisms~~	~~Eqs. (16)~~
~~Spatial differential accuracy~~	~~10th order~~

~~Fig. 11a presents the simulated 6C seismic records for E1 in radial (R), transverse (T), and vertical (Z) coordinates, demonstrating prominent amplitude predominance in the trans.Z and rot.T components. Nonlinear effects manifest as subtle RMS amplitude changes (<1%), with rotational anomalies weaker than~~

~~translational counterparts (Fig. 11b). Normalized time-frequency spectral differences further highlight distinct nonlinear patterns across components and wave phases: direct and reflected waves show larger RMS amplitude changes in trans.R and Z components, while surface waves in trans.T component display the strongest nonlinear sensitivity. S-waves in rot.R and T components and surface waves in rot.Z component show enhanced nonlinear effects, and Love wave nonlinear perturbations in rot.Z component remain relatively weak.~~

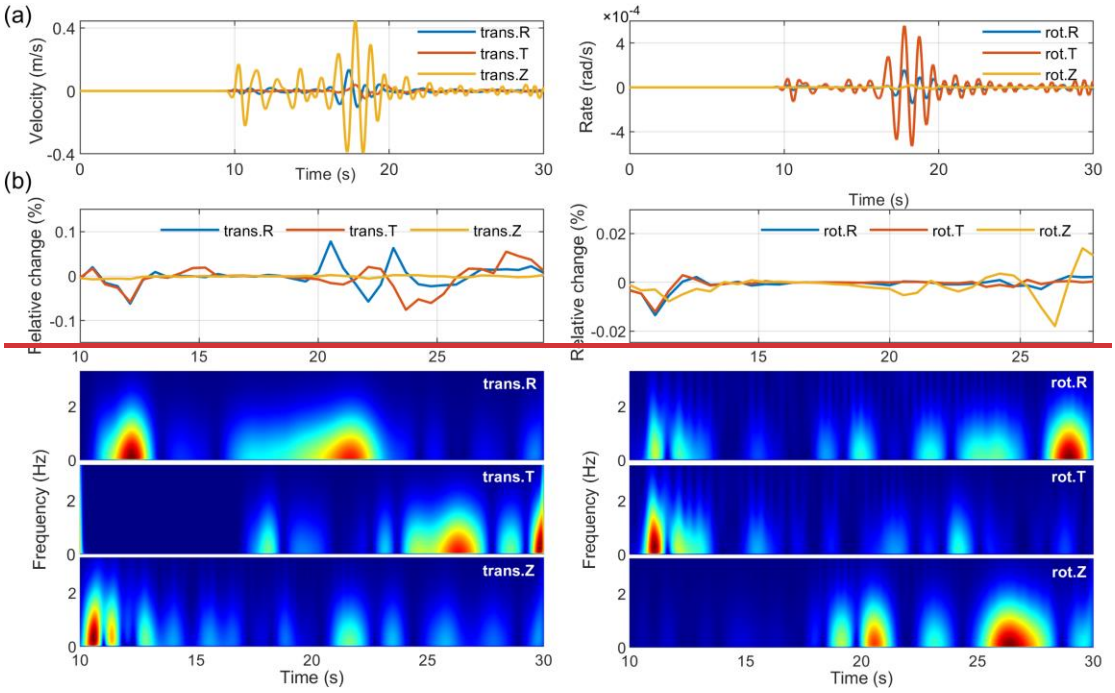

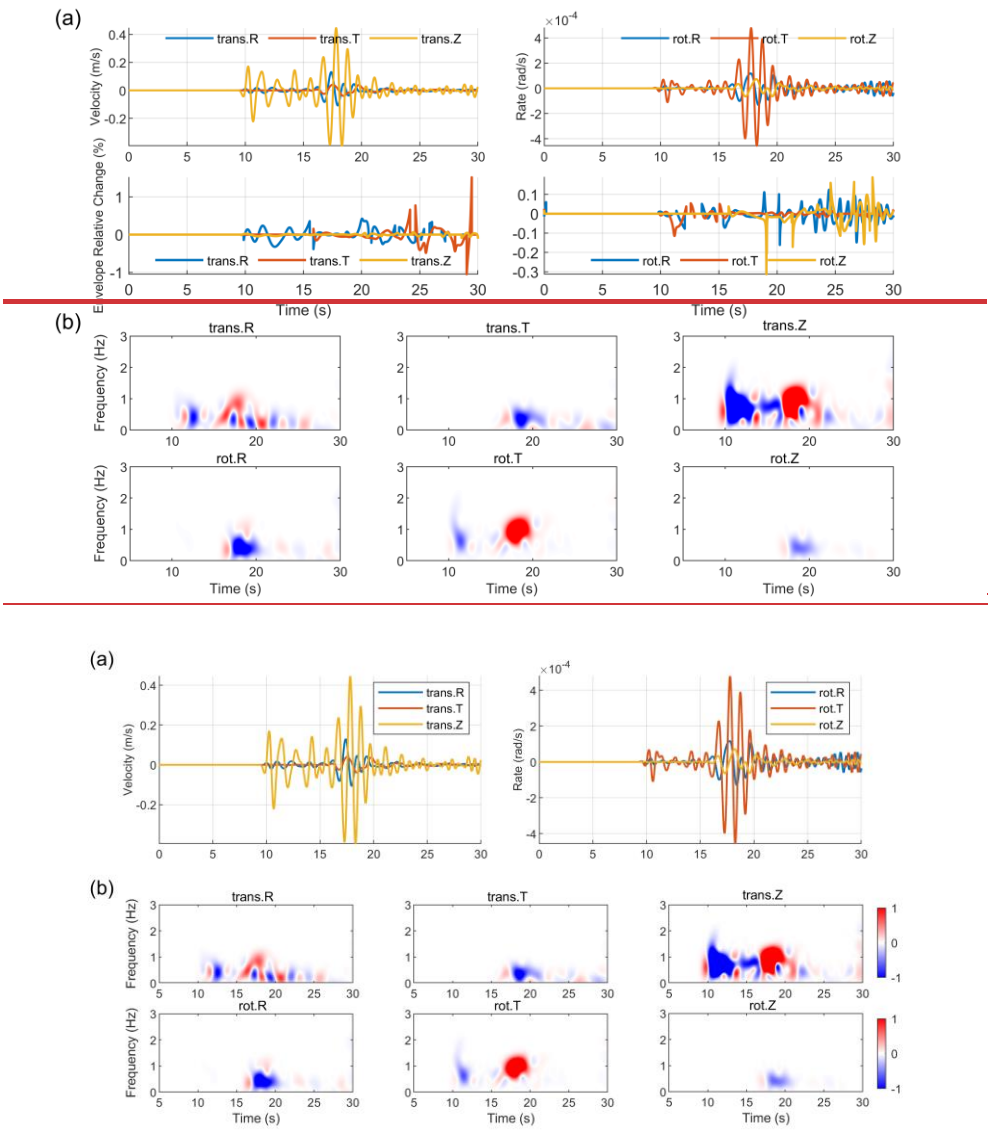

Figure ~~8~~11. (a) Synthetic linear 6C waveforms and (b) normalized time-frequency energy differences (the nonlinear minus the linear) for event E1.

Numerical simulations of the E2 (Fig.9) also show nonlinear effects. Combining the time-domain waveforms (Fig. 9(a)) and the time-frequency energy difference plots (Fig. 9(b)), it can be seen that significant energy changes occur in all components during the arrival of the direct S-wave (approx. 90 s) and the strong surface waves. A long-duration, very-low-frequency (<0.2 Hz) energy enhancement band appears in the

translational components, starting from the surface waves and continuing. This may correspond to long-period perturbations induced by strong surface waves through nonlinear mechanisms, potentially involving P-S coupling in layered media, while the rotational components, as displacement gradients, are not sensitive to it.~~The larger-magnitude E2 simulation demonstrates stronger nonlinear effects, particularly in trans.Z and rot.T components (Fig. 12). Rayleigh waves show pronounced nonlinear distortions, while P-waves in trans.Z and surface waves in trans.R and T components exhibit moderate changes. S-waves and surface waves in the rot.R component are also affected, though rot.Z waveforms display minimal nonlinear alterations.~~

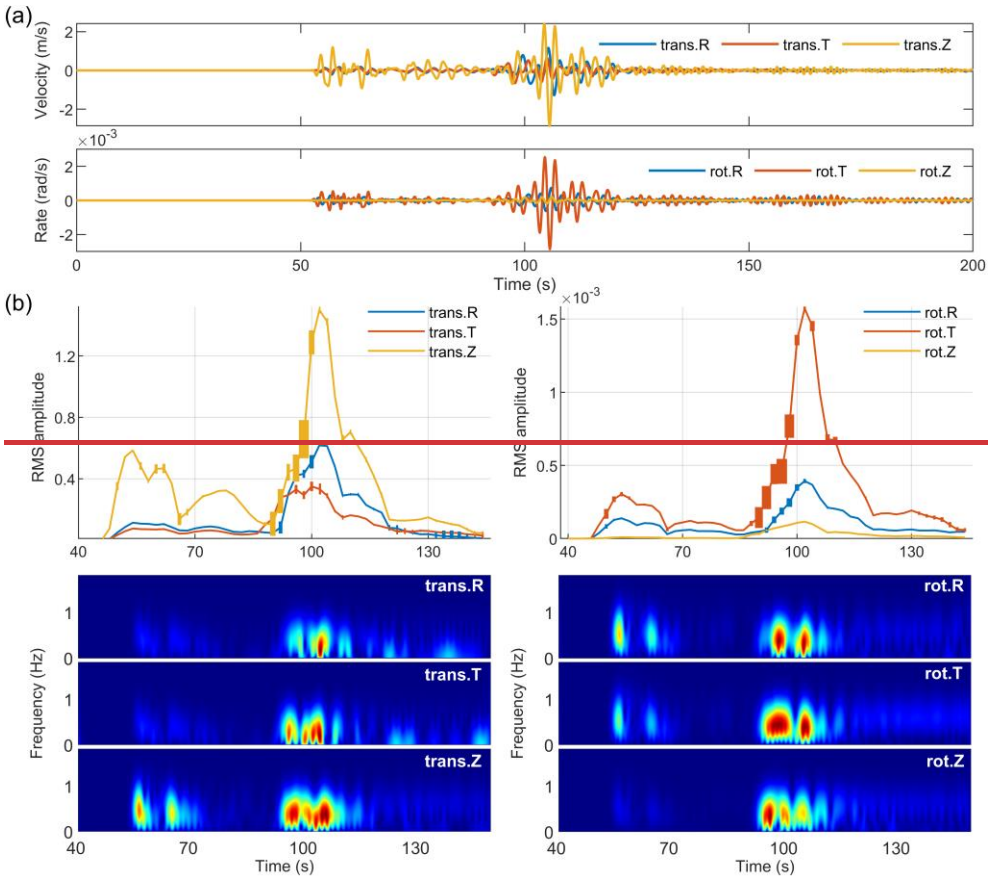

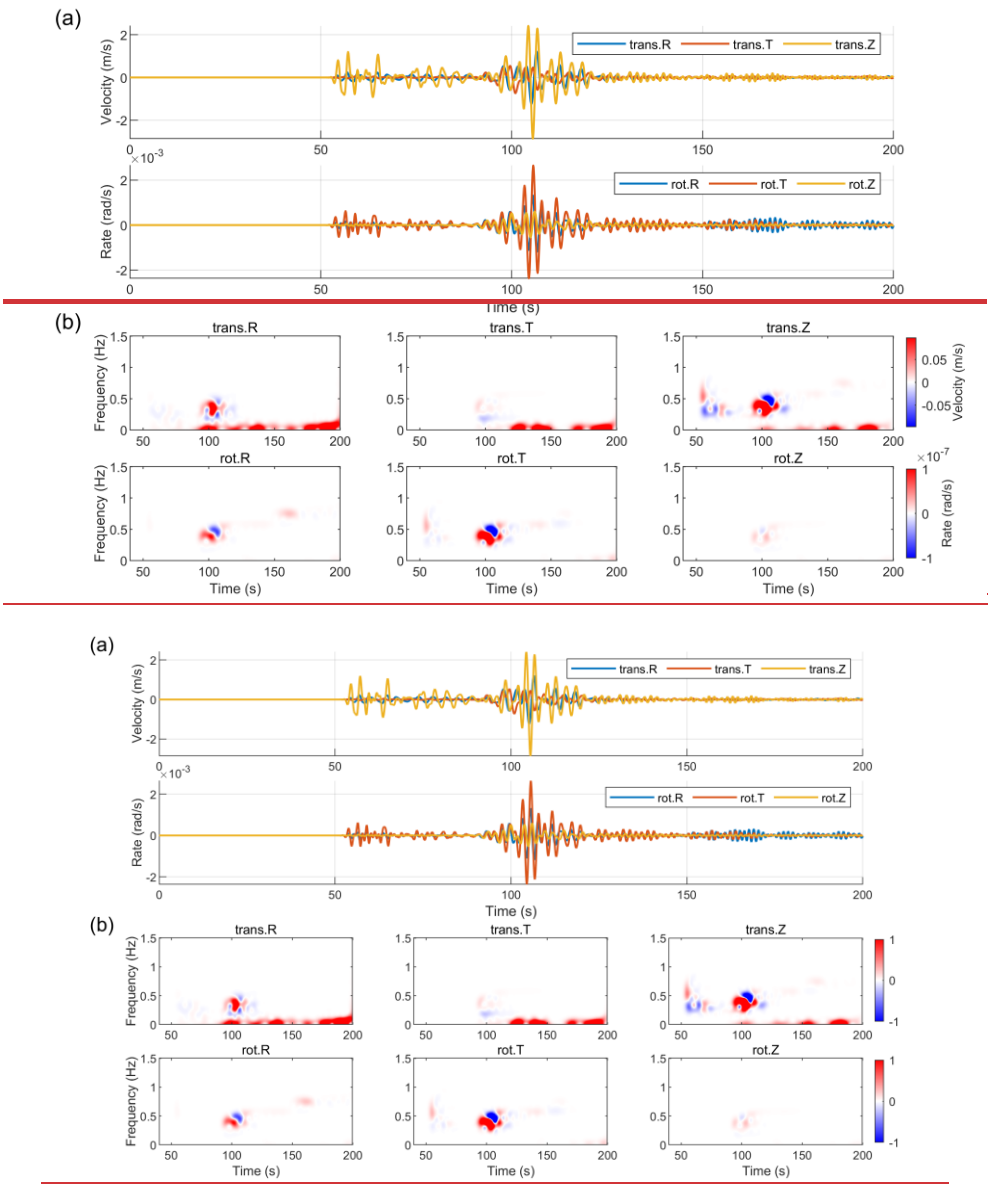

Figure 9~~12~~. (a) Synthetic linear 6C waveforms and (b) normalized time-frequency energy differences (the nonlinear minus the linear) for event E2.~~(a) Synthetic 6C seismic records under linear condition, and (b) RMS amplitude and nonlinear-induced time-frequency spectral difference for E2.~~

By comparing the simulations of the two events, we find that the surface waves are the primary phases that accumulate and carry nonlinear information. At the same time, the E2 event, with its different source mechanism and further propagation path,

exhibits a long-period perturbation not seen in the E1 simulation. This suggests that in more realistic scenarios, the physical mechanisms of nonlinear effects may be more complex and can be influenced by many factors. The different nonlinear characteristics displayed by the two event simulations may also be influenced by the combined effects of their complex, mixed source mechanisms and the specific source-station azimuth.~~The simulations of E1 and E2 reveal some observational implications. For E1, the weak nonlinear effects (<1% amplitude changes) suggest that its receiver location may lie in a region of suppressed nonlinear coupling, likely due to unfavorable source-receiver geometry. In contrast, E2 exhibits stronger nonlinear signatures, particularly in surface waves. This enhanced nonlinear sensitivity in surface waves arises from their inherent P-S interference characteristics, making it a more viable candidate for studying nonlinear effects.~~

~~While rotational Z-component Love waves show minor nonlinear alterations, the translational R/T and rotational R/T components demonstrate more significant changes, particularly in Rayleigh waves. These findings emphasize the need to prioritize specific wave phases and components in future observational data studies. For practical applications, wavefield separation techniques may be necessary to isolate S-waves and surface waves in translational and rotational components, where nonlinear effects are most pronounced.~~

5 Discussion

This study, through systematic simulations of fundamental seismic sources and referenced earthquake events, has demonstrated several characteristics of geometric

nonlinearity in seismic wavefields. First, it demonstrates that the excitation and manifestation of nonlinear effects are controlled by the strain state of the linear wavefield and its spatial gradients. As predicted by nonlinear elastodynamic theory, geometric nonlinearity acts as an equivalent secondary source term in the wave equation, with its strength being proportional to the quadratic terms of the linear strain field. The radiation of nonlinear effects strictly follows the physical nature of longitudinal and transverse waves. For instance, the nonlinear perturbation generated by the strain gradients of a linear P-wave radiates most strongly along the principal direction of the P-wave, whereas the nonlinear rotational effect generated by the shear-strain gradients of an S-wave is most pronounced in regions of maximum S-wave energy. In addition, different source mechanisms (volumetric, pure shear, axisymmetric shear) modulate the mode, strength, and even the effect of the nonlinear response by initializing different geometries of the strain field.

Second, rotational motion is a sensitive indicator for detecting near-field nonlinear effects driven by S-waves. This stems from the physical nature of rotation—it is the spatial gradient of the displacement field and is therefore more sensitive to the secondary source terms driven by strain gradients. This suggests that the deployment and analysis of six-component seismic data are of irreplaceable value for identifying and quantifying nonlinear geophysical processes in future observational studies.

Finally, the simulations of referenced earthquake events show that surface waves, which are more concentrated in energy and have longer propagation paths, are the

primary carriers for accumulating and preserving nonlinear information, thus pointing to a key focus for future observational data analysis. More importantly, in the stronger E2 event, we observed a long-period perturbation not seen in the idealized models. This phenomenon suggests that under realistic strong ground motion conditions, the physical mechanisms of nonlinear effects may be more complex and diverse, potentially involving deeper physical processes such as stress-induced anisotropy. Limitations of this study, such as the use of idealized models, highlight the need for validation with real seismic records. These indicate a direction for future research: how to reliably separate and identify these unique nonlinear signals from collected real seismic records, which is a mixture of complex source effects, 3D heterogeneous propagation effects, and local site responses~~The incorporation of Green strain tensor-based nonlinearity into classical elastodynamic theory introduces higher-order displacement gradient terms (Eqs. (7) and (9)), fundamentally altering seismic wave dynamics by coupling volumetric and shear deformation modes. In linear elasticity theory, volumetric (principal) and shear strains are completely decoupled, and P-wave and S-wave are driven by normal stresses and shear stresses, respectively. While ISO source simulation reveals P-S wave conversion through nonlinear dilatational-shear interactions, the real-world manifestation of such phenomena is constrained by multi-factor geological complexities absent in our idealized models. Future work should prioritize simulations incorporating velocity gradients and attenuation profiles to quantify how propagation paths modulate nonlinear effects, particularly for surface waves where site amplification may enhance nonlinear coupling.~~

~~The differences between E1 and E2 simulations further highlight the need to explore complex source characteristics. While E2's larger magnitude produced clearer nonlinear signatures, most natural earthquakes involve composite rupture dynamics and asymmetric moment tensors. Expanding simulations to include finite-fault sources and spatially varying rupture kinematics could reveal how source complexity interacts with nonlinear strain accumulation.~~

~~Finally, while rotational components show theoretical sensitivity to nonlinear effects, their practical utility remains constrained by observational challenges. Field rotational motions are inherently weaker than translations, and current instruments struggle to resolve most nonlinear changes. Addressing these limitations will require coordinated advances in sensor technology, wavefield separation methods, and targeted field observations focusing on moderate-strong earthquakes where nonlinear effects may cross detection thresholds~~.

6 Conclusions

By incorporating geometric nonlinearity based on the Green-Lagrange strain tensor, this study has conducted 6C seismic wavefield simulations for three fundamental moment tensor sources and two referenced moderate-to-strong earthquakes. The research aims to investigate the characteristics of near-field nonlinear effects and their dependence on source mechanisms. The main conclusions are as follows:~~This work establishes a theoretical and numerical framework for analyzing nonlinear seismic wave propagation through Green strain tensor strain tensor formulations. Numerical simulations of three fundamental seismic moment~~

~~tensor sources (ISO, CLVD, DC) and two moderate-to-strong magnitude earthquakes yield the following key conclusions.~~

(i) Universal radiation pattern of the nonlinear secondary source and source-dependent excitation efficiency. On one hand, the radiation pattern of nonlinearity is universal, strictly adhering to the physics of wave motion: the nonlinear perturbation generated by P-wave strain gradients radiates primarily along the axial direction (a longitudinal characteristic), while the perturbation from S-wave shear-strain gradients radiates mainly in the orthogonal plane directions (a transverse characteristic). This pattern is independent of the initial force source type. On the other hand, the overall efficiency of exciting these nonlinear secondary sources exhibits a strong source-type dependency. Simulation results show that sources with significant shear components, such as CLVD and DC sources, are far more efficient in exciting nonlinear effects than the purely volumetric ISO source.~~Force-source-type dependency: The spatial distribution is intrinsically tied to source kinematics. ISO sources generate overall uniform nonlinear anomalies through volumetric-shear coupling, CLVD sources amplify directional anomalies along principal strain axes of compression/expansion, and DC sources restrict localized nonlinearity to fault-aligned force couple orientations. These patterns arise from how each force source geometry interacts with the nonlinear strain tensor.~~

(ii) High sensitivity of rotational motion to S-wave-driven nonlinearity. This is primarily because rotational motion directly responds to shear-strain gradients, and S-waves are the primary carriers of shear energy. Consequently, rotational motion

744 becomes an ideal window for detecting the secondary sources excited by S-waves,
745 with its nonlinear response being more pronounced than that of translational
746 components.~~Magnitude-energy relationship: Nonlinear effects scale exponentially~~
747 ~~with seismic moment, becoming observationally significant for magnitudes above~~
748 ~~Mw5. At Mw7, rotational components exhibit over 20% relative changes compared to~~
749 ~~linear predictions, whereas changes remain negligible for Mw <4 events. This~~
750 ~~underscores the importance of strain amplitude in triggering detectable nonlinear~~
751 ~~coupling.~~

752 (iii) Effects of wave type and strain level. The strength of nonlinear effects is
753 correlated with the strain level (which can be approximately related to the moment
754 magnitude). More importantly, surface waves, which have more concentrated
755 energy and longer propagation paths, are more effective carriers of nonlinear
756 information than body waves. In the strong-motion event simulation, long-period
757 perturbations, possibly induced by nonlinearity, were also observed. This may
758 correspond to long-period perturbations induced by strong surface waves through
759 nonlinear mechanisms, potentially involving P-S coupling in layered
760 media.~~Rotational motion sensitivity: Rotational components generally demonstrate~~
761 ~~higher nonlinear sensitivity than translational components. Their practical~~
762 ~~detectability depends on source-receiver azimuth.~~

763

764 ~~(iiii) Wave-type specificity: Surface waves exhibit stronger nonlinear signatures than~~
765 ~~body waves in both earthquake simulations, likely due to their inherent P-S~~

~~interference during propagation. However, current models inadequately address surface wave nonlinearity, suggesting unresolved interactions between nonlinear effects and site amplification.~~

Author contributions. WL: conceptualization, methodology, investigation, formal analysis, writing - original draft. YW: conceptualization, writing - original draft and revised draft. CC: investigation, formal analysis. LS: methodology.

Data availability. All data is simulated and available upon reasonable request.

Competing interests. The contact author has declared that neither of the authors has any competing interests.

Disclaimer. Publisher's note: Copernicus Publications remains neutral with regard to jurisdictional claims made in the text, published maps, institutional affiliations, or any other geographical representation in this paper.

Financial support. This research is financially supported by the National Natural Science Foundation of China (No. 42150201、No. 62127815、No. U1839208).

References

Aki, K., and P. G. Richards. Quantitative seismology, 2nd ed, California: University

Science Books, https://doi.org/10.1029/2003EO210008, 2002.

~~Bataille, K., Contreras, M.: Nonlinear elastic effects on permanent deformation due to large earthquakes, Phys. Earth Planet. Inter., 175(1), 47-52, https://doi.org/10.1016/j.pepi.2008.02.016, 2009.~~

Bernauer, M., Fichtner, A., and Igel, H.: Reducing nonuniqueness in finite source inversion using rotational ground motions, J. Geophys. Res.-Solid Earth, 119(6), 4860-4875, https://doi.org/10.1002/2014JB011042, 2014.

Bonilla, L. F., Archuleta, R. J., and Lavallée, D.: Hysteretic and dilatant behavior of cohesionless soils and their effects on nonlinear site response: Field data observations and modeling. Bull. Seismol. Soc. Am., 95(6), 2373-2395. https://doi.org/10.1785/0120040138, 2005.

Bonilla, L. F., Tsuda, K., Pulido, N., Régnier, J., and Laurendeau, A.: Nonlinear site response evidence of K-NET and KiK-net records from the 2011 off the Pacific coast of Tohoku Earthquake. Earth, Planets and Space, 63(7), 785-789. https://doi.org/10.5047/eps.2011.06.012, 2011.

~~Chen, C., Wang, Y., Sun, L. X., Lin, C. J., Wei, Y. x., Liao, C. Q., Lin, B. H.,and Qin, L. P.: Six-component earthquake synchronous observations across Taiwan Strait: Phase velocity and source location, Earth and Space Science, 10, e2023EA003040, https://doi.org/10.1029/2023EA003040, 2023.~~

~~Chen, Q. J., Yin, J. E., and Yang, Y. S.: Time-frequency characteristic analysis of six-degree-freedom ground motion records, Chinese Quarterly of Mechanics, 35, (3), 499-506,~~

~~https://link.oversea.cnki.net/doi/10.15959/j.cnki.0254-0053.2014.03.033, 2014 (in Chinese).~~

~~Dong, L. G., and Ma, Z. T.: A staggered-grid high-order difference method of one-order elastic wave equation, Chinese J. Geophys., 43(3), 411-419, 2000 (in Chinese).~~

Donner, S., Bernauer, M., and Igel, H.: Inversion for seismic moment tensors combining translational and rotational ground motions, Geophys. J. Int., 207(1), 562-570, https://doi.org/10.1093/gji/ggw298, 2016.

Feng, X., Fehler, M., Brown, S., Szabo, T. L., and Burns, D.: Short-period nonlinear viscoelastic memory of rocks revealed by copropagating longitudinal acoustic waves, J. Geophys. Res.-Solid Earth, 123(5), 3993–4006, https://doi.org/10.1029/2017JB015012, 2018.

Frankel, A. D., Carver, D. L., and Williams, R. A.: Nonlinear and linear site response and basin effects in Seattle for the M 6.8 Nisqually, Washington, earthquake. Bull. Seismol. Soc. Am., 92(6), 2090-2109. https://doi.org/10.1785/0120000738, 2002.

Graizer, V. M.: Strong motion recordings and residual displacements: what are we actually recording in strong motion seismology? Seismol. Res. Lett., 8(4), 635-639, https://doi.org/10.1785/gssrl.81.4.635, 2010.

Graizer, V. M.: Inertial seismometry methods, Earth Physics, 27(1), 51-61, 1991.

Graves, R. W.: Simulating seismic wave propagation in 3D elastic media using staggered-frid finite differences, Bull. Seismol. Soc. Am., 86(4), 1091-1106,

1996.

Gilbert, F.: Excitation of the normal modes of the Earth by earthquake sources, Geophys. J. R. astr. Soc, 22(2), 223-226, https://doi.org/10.1111/j.1365-246X.1971.tb03593.x, 1970.

~~Guyer, R. A., and Johnson, P. A.: Nonlinear mesoscopic elasticity: evidence for a new class of materials, Physics Today, 52(4), 30-36, https://doi.org/10.1063/1.882648, 1999.~~

Hua, S. B., and Zhang, Y.: Numerical experiments of moment tensor inversion with rotational ground motions, Chinese J. Geophys., 65(1), 197-213, https://doi.org/10.6038/cjg2022P0668, 2022 (in Chinese).

Huras, L., Zembaty, Z., Bonkowski, P. A., and Bobraet, P.: Quantifying local stiffness loss in beams using rotation rate sensors, Mech. Syst. Signal Proc., 151, 107396, https://doi.org/10.1016/j.ymssp.2020.107396, 2021.

Ichinose, G. A., Ford, S. R., and Mellors, R. J.: Regional moment tensor inversion using rotational observations, J. Geophys. Res.-Solid Earth, 126(2), e2020JB020827, https://doi.org/10.1029/2020JB020827, 2021.

~~Jia, L., Yan, S. G., Zhang, B. X., and Huang, J.: Research on perturbation method for nonlinear elastic waves, J. Acoust. Soc. Am., 148, EL289-EL294, https://doi.org/10.1121/10.0001980, 2020.~~

Jost, M. L., and Hermann, R. B.: A students guide to and review of moment tensors, Seism. Res. Lett., 60, 37-57, https://doi.org/10.1785/gssrl.60.2.37, 1989.

Knopoff, L., and Randall M. J.: The compensated linear-vector dipole: A possible

mechanism for deep earthquakes, J. Geophys. Res., 75(26), 4957–4963, https://doi.org/10.1029/JB075i026p04957, 1970.

Kozak, J. T.: Tutorial on earthquake rotational effects: historical examples, Bull. Seismol. Soc. Am., 99(2B), 998-1010, https://doi.org/10.1785/0120080308, 2009.

Laske, G., Masters, G., Ma, Z. T., and Pasyanos, M.: Update on CRUST1. 0-A 1-degree global model of Earth's crust, EGU General Assembly 2013, 15, EGU2013-2658, 2013.

Lee, W. H. K., Igel, H., Todorovska, M. I., and Trifunac, M. D.: Recent advances in rotational seismology, Seismol. Res. Lett., 80(3), 479–490, https://doi.org/10.1785/gssrl.80.3.479, 2009.~~Lee, C. E. B., Celebi, M., Todorovska, M. I., and Diggles, M. F.: Rotational seismology and engineering applications — Proceedings for the First International Workshop, Menlo Park, California, U.S.A. September 18 to 19, 2007: U.S. Geological Survey Open-File Report 2007-1144, 46 p. http://pubs.usgs.gov/of/2007/1144/, 2007.~~

Li, H. N.: Study on rotational components of ground motion, Journal of Shenyang Architectural and Civil Engineering Institute, 7(1), 88-93, 1991 (in Chinese).

Li, H. N., and Sun, L. Y.: Rotational components of earthquake ground motions derived from surface waves, Earthq. Eng. Eng. Vib., 21(1), 15-23, https://link.oversea.cnki.net/doi/10.13197/j.eeev.2001.01.003, 2001 (in Chinese).

Li, P. X., Lin, W. J., Zhang, X. M., Wang, X. M.: Comparisons for regular splitting and non-splitting perfectly matched layer absorbing boundary conditions. Acta

Acustica, 40(01), 44-53, https://link.oversea.cnki.net/doi/10.15949/j.cnki.0371-0025.2015.01.006, 2015.

Madariaga, R.: Dynamics of an expanding circular fault, Bull. Seismol. Soc. Am., 66(3), 639-666, https://doi.org/10.1007/BF02246368, 1976.

McCall, K. R.: Theoretical study of nonlinear elastic wave propagation, J. Geophys. Res., 99(B2), 2591-2600, https://doi.org/10.1029/93JB02974, 1994.

Moczo, P., Robertsson, O. J., and Eisner, L.:The finite-difference time-domain method for modeling of seismic wave propagation, Advances in Geophysics, 48, 421-516. https://doi.org/10.1016/S0065-2687(06)48008-0, 2007.

Oliveira, C. S., and Bolt, B. A.: Rotational components of surface strong ground motion, Earthq. Eng. Struct. D. 18(4), 517-526, https://doi.org/10.1002/eqe.4290180406, 1989.

Pei, Z. L.: Numerical simulation of elastic wave equation in 3-D anisotropic media with staggered-grid high-order difference method, Geophysical Prospecting for Petroleum, 44(4), 308-315, https://doi.org/10.3969/j.issn.1000-1441.2005.04.002, 2005 (in Chinese).

Régnier, J., Bonilla, L. F., Bard, P. Y., et al.: PRENOLIN: International benchmark on 1D nonlinear site-response analysis—Validation phase exercise. Bul. Seismol. Society of America, 108(2), 876-900. https://doi.org/10.1785/0120170210, 2018.

Renaud, G., Le Bas, P. Y., and Johnson, P. A.: Revealing highly complex elastic nonlinear (anelastic) behavior of Earth materials applying a new probe: Dynamic

acoustoelastic testing, J. Geophys. Res.-Solid Earth, 117, B06202, https://doi.org/10.1029/2011JB009127, 2012.

Renaud, G., Rivière, J., Le Bas, P. Y., and Johnson, P. A.: Hysteretic nonlinear elasticity of Berea sandstone at low-vibrational strain revealed by dynamic acoustoelastic testing, Geophys. Res. Lett., 40(4), 715-719, https://doi.org/10.1002/grl.50150, 2013.

Sun, L., Yu, Y., Lin, J. Q., and Liu, J. L.: Study on seismic rotation effect of simply supported skew girder bridge, Earthquake Engineering and Engineering Dynamics, 37(4), 121-128, https://doi.org/10.13197/j.eeev.2017.04.121.sunl.014, 2017 (in Chinese).

Sun, L. X., Zhang, Z., and Wang, Y.: Six-component elastic-wave simulation and analysis, EGU General Assembly 2018, Geophysical Research Abstracts, 20, EGU2018-14930-1, 2018.

TenCate, J. A., Malcolm, A. E., Feng, X., and Fehler, M. C.: The effect of crack orientation on the nonlinear interaction of a P wave with an S wave, Geophys. Res. Lett., 43(12), 6146-6152, https://doi.org/10.1002/2016GL069219, 2016.

Tromp, J., and Trampert, J.: Effects of induced stress on seismic forward modelling and inversion. Geophys. J. Int., 213(2), 851-867. https://doi.org/10.1093/gji/ggy020, 2018.

Virieux, J.: P-SV wave propagation in heterogeneous media; velocity-stress finite-difference method, Geophysics, 51(4), 889-901, https://doi.org/10.1190/1.1442147, 1986.

~~Wang, L., Luo, Y. H., and Xu, Y. H.: Numerical investigation of Rayleigh wave propagation on topography surface, J. Appl. Geophys., 86, 88–97, https://doi.org/10.1016/j.jappgeo.2012.08.001, 2012.~~

~~Wessel, P., Luis, J. F., Uieda, L., Scharroo, R., Wobbe, F., Smith, W. H. F., and Tian, D.: The generic mapping tools version 6, Geochemistry, Geophysics, Geosystems, 20, 5556–5564, https://doi.org/10.1029/2019GC008515, 2019.~~

Xu, Y. X., Xia, J. H., and Miller, R. D.: Numerical investigation of implementation of airearth boundary by acoustic-elastic boundary approach, Geophysics, 72 (5), SM147–SM153, https://doi.org/10.1190/1.2753831, 2007.

Yan, Y. Y.: Seismic response analysis of high-rise building under different types of multi-dimensional earthquake ground motions (Ph.D. dissertation), Jiangsu University, 2017(in Chinese).

~~Yu, S. B., Kuo, L. C., and Punongbayan, R. S., Emmanuel, G.R.: GPS observation of crustal deformation in Taiwan-Luzon region, Geophys. Res. Lett., 26(7), 923–926, https://doi.org/10.1029/1999GL900148, 1999.~~

~~Yang, D. H., Liu, E., Zhang, Z.J., and Teng, J.: Finite-difference modelling in two-dimensional anisotropic media using a flux corrected transport technique, Geophys. J. Int., 148(2), 320–328, https://doi.org/10.1046/j.0956-540x.2001.01575.x, 2002.~~

~~Zheng, H. S., Z. J. Zhang, and Liu, E. R.: Nonlinear seismic wave propagation in anisotropic media using the flux-corrected transport technique, Geophys. J. Int., 165(3), 943–956, https://doi.org/10.1111/j.1365-246X.2006.02966.x, 2006.~~

941 Zhou, C., Zeng, X. Z., Wang, Q. L., ~~and~~ Liu, W. Y., and Wang, C. Z.: Rotational
942 motions of the Ms7.0 Jiuzhaigou earthquake with ground tilt data, Science China
943 Earth Science, 62(5), 832-842, https://doi.org/10.1007/s11430-018-9320-3, 2019.